
# NEUTRONS IN PROTON THERAPY

Quantifying the spatial and angular distribution of lethal neutrons for treatment planning

ABSTRACT

It is known that high energy protons in proton therapy generate secondary particles. Of which, secondary neutrons are a main concern as they deposit out-of-field doses and can have long-term health effects on cancer patients. In this report, the energy, 3-D spatial and angular distribution of the production yield of neutrons are scored along the proton beam path in different types of tissue medium. The degree of biological damage is then quantified through factoring in the relative biological effectiveness of neutrons. This systematic study involved simulating 70, 150 and 200 MeV proton beam transport in various tissue compositions in GEANT4. System specifications of the Hitachi proton therapy system were used in this study. Simulation results showed that the neutrons are forward facing and are generally emitted at a preferential angle. With considerations on the RBE variation with neutron's energy, the spatial and angular distribution of the production of lethal neutrons were identified along the proton track. Non-trivial relations between biological damage in different tissue medium were observed. Such comprehensive simulation studies have not been reported and this input information can be useful for treatment planning in reducing out-of-field neutron dose in sensitive organs and increase the dose deposited into the tumor.

Jonathan Yeo Jian Wei
A0125932H

# Acknowledgements

I would like to express my deepest gratitude towards my supervisor, Dr. James Lee, co-supervisor, A/P Andrew Bettiol and Ang Khong Wei for the great advice and support they have given in the past year. I would like to specially thank my mentor, Tan Hong Qi, for all that he has done in the past year; the guidance he has given me for my final year project, and his advice on academics and career choices. Without his guidance, I would not have the many opportunities that await me after my graduation.

# Contents

1 Introduction ..... 1

1.1 Radiation in Cancer Treatment ..... 1

1.2 Proton Therapy ..... 2

1.3 Risk of Secondary Cancer ..... 3

1.4 Secondary Particles: Possible Cause of Secondary Cancer ..... 4

1.5 Neutrons ..... 5

1.6 Relative Biological Effectiveness ..... 6

1.7 Current Research ..... 8

1.8 My work ..... 9

2 Materials and Methods ..... 10

2.1 Simulation Geometry ..... 10

2.2 Physics Model ..... 11

2.3 Tissue Phantoms ..... 12

2.4 Angular Distribution ..... 12

2.5 Lethality Factor ..... 13

2.6 Data Analysis ..... 13

3 Results and Discussion ..... 14

3.1 Proton Beam Dose Distribution ..... 14

3.2 Spatial Distribution of Neutrons ..... 16

3.3 Spatial Distribution of the Neutron Energies ..... 17

3.4 Energy Distribution of Neutrons ..... 20

3.5 Angular Distribution of Neutrons ..... 21

3.6 Varying Tissue Medium ..... 23

3.7 Lethality ..... 27

4 Comparison between Physics Models ..... 30

5 Neutron Transport ..... 34

6 Conclusion ..... 36

7 Future Works ..... 37

8 Appendix ..... 40

# 1 Introduction

Radiation is a double-edged sword that can be used for detecting and eliminating cancer. However, it must be well managed and carefully planned as it comes with an added risk of side effects that can become apparent soon after the exposure or resurface many years later in the form of secondary cancer. To reduce the risk of such effects, clinicians must identify the best ways to achieve best tumour control, while reducing normal tissue complications. This can be achieved through careful treatment planning and research.

The research in this paper investigates the risk of biological damage from the secondary neutrons produced during proton therapy. This would provide information for treatment planning to reduce the out-of-field neutron dose and increase the dose deposited into the tumour. The research is conducted through simulation of the transport of proton beams of various energies through a selection of tissue phantoms in GEANT4 [1]–[4]. This thesis introduces a new quantity known as lethality, to quantify the risk associated with the secondary neutrons produced.

## 1.1 Radiation in Cancer Treatment

There are several uses of radiation in cancer treatment. Some examples are radiotherapy, proton therapy and brachytherapy.

X-ray radiotherapy is a form of cancer treatment where x-ray photons are targeted towards a cancer tumour, to deposit radiation dose and kill the cancer cells. The photons interact with matter via electromagnetic interactions, namely, the photoelectric effect, Compton scattering and pair production, which results in the photons being scattered or absorbed. Consequently, the photons are attenuated along its path length and deposits its dose following an attenuation curve represented in Fig. 1 [5]. This means that the dose delivered is highest when the beam enters the body and reduces as the x-ray beam travels along the body.

## 1.2 Proton Therapy

Proton therapy uses protons instead of photons, and is another form of cancer treatment that has been gaining popularity in recent years. With the completion of the Goh Cheng Liang Proton Therapy Centre in 2022 [6], Singaporeans would also have the choice of proton therapy as a treatment option.

One benefit of proton therapy over conventional x-ray radiotherapy is the ability to administer a high dose of radiation into region where the cancer tumour resides and a smaller dose to the healthy tissues along the proton beam path [7], hence reducing the risk of secondary cancer. This property arises from the interaction between protons and matter, where the proton deposits its energy in a way that forms a Braggs peak shown in Fig. 1 [5]. This means that the dose delivered is lowest when the beam first enters the body and remains low, up till the point just before the beam stops where there is a sharp increase in the delivered dose. Consequently, there is no dose deposited after the Braggs peak.

The depth in which the Braggs peak occurs is dependent on the initial energy of the proton, allowing radiation oncologists to localize the dose deposition by selecting a suitable beam energy according to the location of the cancer tumour [7].

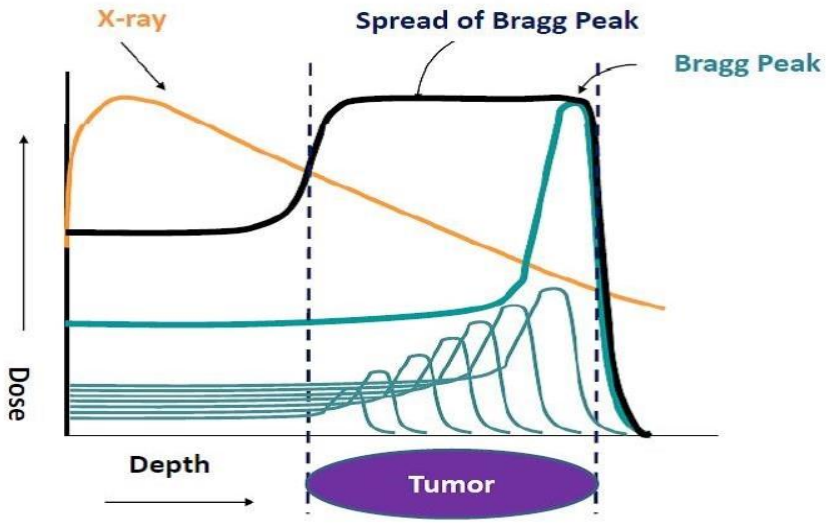


Fig. 1. Comparison of the dose deposition characteristics between proton beam and X-ray. Image taken from: [5].

## 1.3 Risk of Secondary Cancer

The claim that proton therapy reduces the risk of secondary cancer, as compared to x-ray radiotherapy, has been supported by studies [8]–[10]. These studies showed a reduction in secondary cancer occurrences in patients that underwent proton therapy as compared to radiotherapy. However, it is important to note that because proton therapy is relatively new, more research and a longer follow up is required to come to any conclusion on the actual decrease in risk.

The statistics showing the secondary cancer recurrence rate from the three studies mentioned can be found in Table 1.

**Table 1.** Statistics of secondary cancer recurrence in patients that underwent either proton therapy and radiotherapy

| Reference | Type of Cancer | Proton | Photon |
|---|---|---|---|
| Sethi et. al. (2013) DOI:10.1002/cncr.28387 | Retinoblastoma (eye) | 1/55 (1.8%) | 4/31 (12.9%) |
| Chung et. al. (2013) DOI:10.1016/j.ijrobp.2013.04.030 | Prostate, central nervous system or head region (pediatric) | 29/558 (5.2%) | 42/558 (7.5%) |
| Eaton et. al. (2015) DOI:10.1016/j.ijrobp.2015.09.014 | Medulloblastoma (brain) | 0/45 (0%) | 3/43 (7.0%) |

In the first paper, Sethi et. al. followed a group of people that had retinoblastoma treatment with either protons or photons for a certain number of years [8]. Their results showed that 1 out of 55 patients that had proton therapy developed an osteosarcoma of the distal femur (bone cancer), while 4 out of 31 patients that had radiotherapy developed secondary cancers at the sinus, bone, neck, brain years later.

Chung et. al. followed a larger group of children and found that 5.2% of the people that had proton therapy developed a secondary cancer. This is a drop from the 7.8% of people that had radiotherapy [9].

Eaton et. al. followed a group of patients that underwent treatment for medulloblastoma, and no patients that went through proton therapy reported secondary cancer. 3 out of 43 patients that had radiotherapy, however, developed secondary cancer years later [10].

From the above, all three papers show a reduction in the rate of secondary cancer in proton therapy treatment as compared to x-ray radiotherapy.

However, it is important to note that in addition to the reduced risk, all the secondary cancer developed at a secondary site away from the primary cancer. A possible suspect for the development of secondary cancer is the out-of-field doses from the treatment. Although it is also possible that the secondary cancer developed through other radiobiological reasons, such as an increase in metastatic potential, we should not neglect the out-of-field doses in treatment planning.

## 1.4 Secondary Particles: Possible Cause of Secondary Cancer

Though there is a reduction in the number of secondary cancer occurrence between proton therapy and radiotherapy, there are still reported cases of secondary cancer from proton therapy. These reported cases of secondary cancer occur at a secondary site from the primary cancer, and it is possible that the secondary cancer is caused by the out-of-field dose from proton therapy.

The secondary particles generated during the non-elastic nuclear interaction of the proton and matter, in proton therapy, can be a possible source of the out-of-field dose [11]. When a proton travels through a medium, it can undergo electronic interaction or nuclear interaction. Protons are mostly slowed down through electronic coulomb interaction and scattered/absorbed through the nuclear interactions, generating secondary particles in the process. Secondary protons, deuterons, neutrons and prompt gammas are possible secondary particles that can be emitted from the nuclear interaction.

Out of these particles, secondary protons and deuterons are less of a concern as they often have a short path length and contribute to the in-field dose. Neutrons and prompt gammas, however, have a longer path length and can contribute to the out-of-field dose. Moreover, neutrons can be dangerous because of their high Relative Biological Effectiveness (RBE) and high Linear Energy Transfer (LET) properties [12]. As such, a small absorbed dose may lead to DNA damage [12].

## 1.5 Neutrons

Neutrons are uncharged particles that do not undergo coulomb interaction and lose their energy mainly through elastic nuclear scattering. The effect a neutron experiences from an electronic interaction is negligible due to it being uncharged. This is the reason why neutrons have a longer mean free path as compared to charged particles.

Neutrons can be classified into different categories depending on its energy. This would allow us to identify if the neutron will interact with the material, because the interaction cross section of neutron is strongly dependent on the energy of the particle [13]. To illustrate how the cross section changes with the energy of the particle, the interaction cross section of the elastic collision of neutrons, with Hydrogen-1, is presented in Fig. 2 [14].

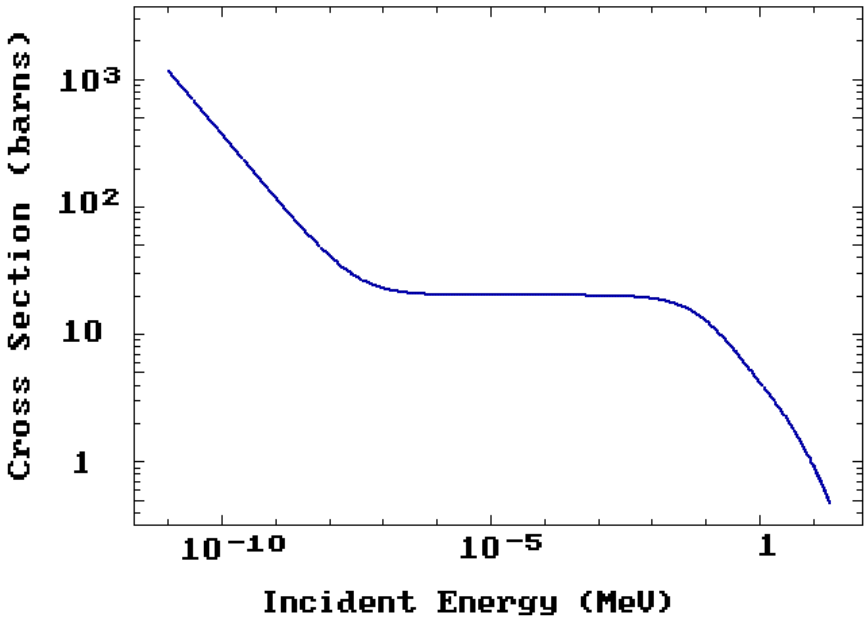


**Fig. 2.** Graph of the interaction cross section of the elastic collision of neutrons with Hydrogen-1 with respect to the energy of the neutron. Data taken from [14].

The energy of the neutrons produced in proton therapy can span a wide range of energies, from ultrafast neutrons (> 20 MeV) to thermal/cold neutrons (0 eV – 0.025 eV). However, in our study, intermediate neutrons (300 eV – 1 MeV) are the most concerning type of neutrons due to their high Relative Biological Effectiveness (RBE).

This means that they can cause a high amount of biological damage to tissues and may result in DNA damage.

## 1.6 Relative Biological Effectiveness

Relative Biological Effectiveness (RBE) is defined as the ratio of the doses required by two radiations to cause the same level of effect. It is an empirical value that converts absorbed dose into a biological equivalent dose.

The RBE value differs across various ionizing radiation because different ionizing radiation interacts with matter differently. Protons, for example, have an RBE value close to 1.1 [15].

At the point of writing, the international regulatory commission, International Commission on Radiological Protection (ICRP) has agreed upon a set of RBE values for neutrons of different energies [16]. However, the ICRP standard assumes a low neutron dose and states that the standard is only applicable for radiation protection purposes and is not suitable to be used for the assessment of risk [13]. In this paper, the RBE values used are determined based on the quantification of the DNA double strand break clusters simulated by Baiocco et. al. using the Particle and Heavy Ion Transport code System (PHITS) and monte carlo simulation, PARTRAC [13]. The graph of neutron RBE vs energy is presented in Fig.3.

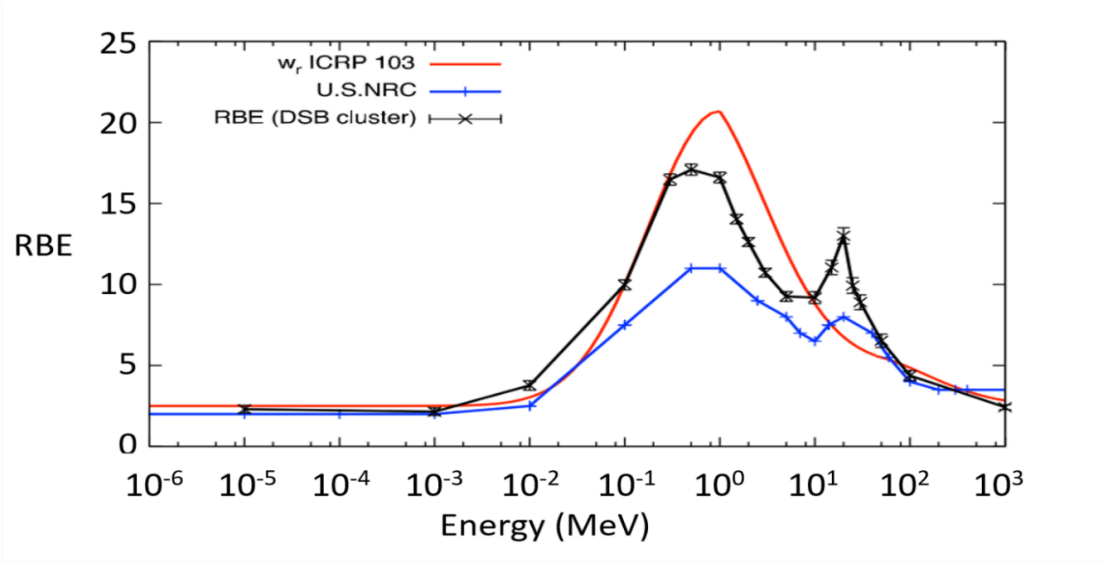


**Fig. 3.** Graph of Neutron RBE as a function of energy obtained using DSB cluster induction (black), ICRP (red) and U.S. NRC (blue). Error bars on RBE are from DSB cluster induction come from errors on the DSB cluster yields. Image adapted from: [13].

The RBE value calculated based on the number of DNA double strand breaks is a better representation of the risk of secondary cancer, than the ICRP standard, because double strand breaks constitute a large risk towards cancer, although many other factors such as the DNA repair mechanisms of the cell do play a role [13]. However, until we fully understand the mechanisms behind cancer development, the RBE values based on double strand break clusters serve as a good approximation of the relative damage caused.

In addition to having a high RBE, neutrons also have a high LET coefficient [12], meaning that they deposit higher concentration of doses along the neutron path as compared to electrons or gamma photons, that have a low LET. This is because the mass of a neutron is close to the mass of a hydrogen atom, which is abundant in tissues. As a result, each elastic collision with a hydrogen atom transfers a large percentage of the neutron energy and momentum to the atom.

We can assess the risk of biological damage and secondary cancer from the secondary neutrons produced in proton therapy by considering these factors and the nuclear interaction cross section of neutrons.

## 1.7 Current Research

The risk of secondary cancer from secondary neutrons produced in proton therapy treatment have been studied by several research groups in the past [11], [12], [17], [18].

In one of the studies, researchers investigated the risk of secondary cancer, induced from neutrons produced in passive modulation proton therapy machine [17], [18]. These neutrons are produced when the proton beam scatters off a scattering foil that is used to widen the proton field.

Results from both papers showed an increased risk from the secondary neutron-induced secondary cancer, when a passive proton therapy machine is used instead of an active proton therapy machine. This is because a passive proton therapy machine uses scattering foils to direct the beam, and the scattering of protons from the foils creates a significant number of neutrons. This is compared to an active proton therapy machine, which uses magnetic scanners to direct the beam [17], [18].

Another study simulated the dose due to secondary neutrons and photons in proton therapy treatment of the eye and deep-seated tissues using the *FLUktuierende KAskade* (FLUKA) code [11]. Their results found that the dose contributions due to secondary neutrons and photons are $10^{-4}$ Gy for the treatment of eye tumour using a passive proton beam system, $10^{-2}$ Gy for the treatment of deep seated tumour using a passive proton beam system and $10^{-3}$ Gy when treating deep seated tumour with an active proton beam system.

These studies present several methods of secondary cancer risk estimation models. They often compare the risk from proton therapy and the risk associated with x-ray radiotherapy methods. However, none of these studies considered the neutrons created from different tissues within the human body.

This is a cause for concern because the interaction of protons with tissues do create secondary neutrons. Moreover, at the time of writing, commercial proton therapy

treatment planning systems do not have the capabilities to determine neutron doses, and hence neutron doses are often neglected.

## 1.8 My work

Hence, we conducted a comprehensive study of neutron production in various tissue medium to provide information of the angular distribution, spatial distribution and energy distribution of these secondary neutrons created in the tissues. The study was conducted using a Monte Carlo simulation in GEANT4. This information would allow treatment planners consider the risks associated with secondary neutrons in proton therapy. This information would also allow treatment planners to understand if the neutrons produced from proton therapy is sufficiently high for Boron-11 to act as an effective radiosensitiser to increase the dose deposited in the tumour region through capturing of the neutrons.

In addition, this thesis compares the lethality factor among various tissue medium to quantify the possible risk of DNA damage caused by the production of neutrons. We will also provide a short section on the transport of the neutrons and compare the differences between the Bertini physics model and the binary cascade physics model that can be used for the simulation.

# 2 Materials and Methods

To perform the study, a Monte Carlo simulation, derived from GEANT4, was used to simulate the yield of neutrons produced during proton therapy on various tissue models available from the GEANT4 materials database. This simulation was originally developed for the commissioning of the upcoming proton therapy centre in Singapore.

Proton pencil beams of energies 70 MeV, 150 MeV and 200 MeV were used in this study to monitor the secondary neutron production in various blocks of 30 x 30 x 30 cm tissue phantoms. A total of 10 million protons were simulated in each run. The energy, momentum and position of the secondary neutrons were scored and analysed. Transport of the neutrons were killed right after production, to reduce the computing power and size of the data; the information of the neutron transport is not required because of the sole interest in the initial state parameters of the neutrons.

## 2.1 Simulation Geometry

The proton therapy system in the simulation was configured based on the specifications of the Hitachi Proton Therapy system, that will be built in the Goh Cheng Liang Proton Therapy Centre. The nozzle and detector geometry are constructed in GEANT4 using the G4VUserDetectorConstruction class. Components such as range shifter, main and sub dose monitor, beam position monitor and the Kapton window, that are used in scanning proton therapy, are added into the nozzle geometry. These components affect the beam profile through the introduction of longitudinal and lateral straggling. A schematic diagram of the proton therapy nozzle and detector geometry is presented in Fig. 4. In our geometry, a magnetic scanner was used instead of a scattering foil to direct the proton beam. This mimics the Hitachi system, which is an active proton therapy system instead of a passive one.

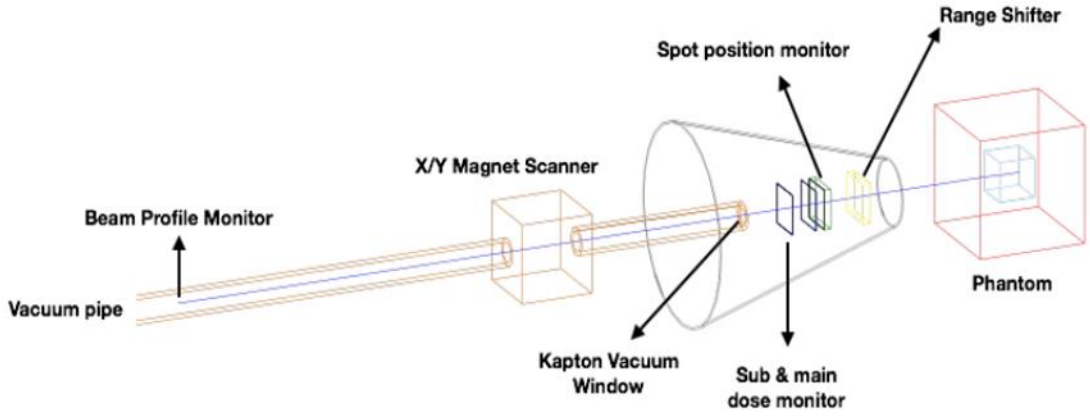


**Fig. 4.** Schematic diagram of the nozzle and detector geometry used for simulation. The beam starts at the Beam Profile Monitor (BPM) and transverse through the Kapton window, sub and main dose monitor, beam position monitor and finally range shifter before hitting the tissue phantom.

The beam path starts at the Beam Profile Monitor (BPM), as determined by the phase space parameters provided by Hitachi. The beam then passes through a 30 x 30 x 30 cm tissue phantom centred at the isocentre. The position, momentum and energy of the secondary neutrons generated through the interaction of the proton with the tissue phantom are then recorded for analysis.

## 2.2 Physics Model

In the simulation, the QGSP_BIC_EMY physics model was used. The G4HadronPhysicsQGSP_BIC physics model [19] in GEANT4 was used to obtain the data of the neutron's position and momentum.

The Quark-Gluon String Pre-compound (QGSP) physics model was chosen because it is highly recommended for medical application [19]. The QGSP model can simulate nuclear excitation through high energy interactions and subsequently the nuclear de-excitation, using the pre-compound model and generate secondary particles, making it suitable for the study.

The Binary Cascade (BIC) component [20] in the model replaces the original Low Energy Parameterised (LEP) model in QGSP with a binary cascade, and is used because

it is better at describing the production of secondary particles produced in the interactions of protons with the nuclei.

The electromagnetic model used was the EMY option, which refers to the emstandard_opt3 in the electromagnetic model and was chosen to achieve a higher accuracy because it can give the most precise description of low energy effects.

## 2.3 Tissue Phantoms

A total of 24 blocks of tissue phantoms were used for this study, and the neutron yield from each phantom were compared against each other. The tissue phantom materials were constructed based on National Institute of Standards and Technology (NIST) tissue standards that are present in the GEANT4 materials database [4]. Each phantom is made up of a 30 x 30 x 30 cm block of tissue, ranging from bone to adipose tissues. The full list of the tissue models used can be found in Table 2 and 3.

## 2.4 Angular Distribution

The angular distribution was determined based on the information of the momentum vector of the neutrons. The angle of the direction of the neutron was calculated from the direction of pencil beam using the Eq. (1) and Eq. (2),

$$\theta = \cos^{-1}\frac{P_x}{\sqrt{P_x^2 + P_y^2 + P_z^2}} \quad (1)$$

$$\phi = \tan^{-1}\frac{P_y}{P_z} \quad (2)$$

where $P_x$, $P_y$, $P_z$ are the momentum of the neutron in the x, y and z direction respectively. In our calculations, the x direction refers to the direction in which the beam travels.

A visual representation the angles can be found in the appendix.

## 2.5 Lethality Factor

In this study, a lethality factor was defined as the track-summed RBE of the neutrons in each voxel of 1.5 x 1.5 x 1.5 $mm^3$. The lethality factor is a measure of the maximum risk of localized DNA damage from neutrons at the moment of production, and it follows Eq. (3),

$$L(i) = \sum_{E} R_E \times N_{E,i} \tag{3}$$

where $R_E$ is the Relative Biological Effectiveness value of the neutron based on its energy, $N_{E,i}$ is number of neutrons of energy E in the *i*-th voxel and *L(i)* is the sum across all neutron energies in the *i*-th voxel to obtain the lethality factor.

The RBE values of the neutrons used in this paper considers double strand break clusters caused by the neutrons and is dependent on the energy of the neutrons [13]. The total lethality is then calculated by summing up the lethality values of all the voxels in one run.

## 2.6 Data Analysis

After running the GEANT4 simulation, the data generated by the system was recorded in two separate output files. One of the files contain the spatial distribution of the dose detected by the detector geometry in the phantom, and is named “Dose.out”, while another file contains the position, momentum and energy of the secondary neutron at the moment it is created by the system.

A total of 72 runs, consisting of 3 beam energies (70 MeV, 150 MeV, 200 MeV) incident on 24 different tissue phantoms, were conducted, simulating the neutron production in each run. The results from each run were collated, analysed using MATLAB R2016a and Wolfram Mathematica 10, and are presented in the next chapter.

# 3 Results and Discussion

This chapter presents the results and discussion on the properties of the secondary neutrons, and the risks associated with it.

## 3.1 Proton Beam Dose Distribution

In the first section, we will analyse and discuss the distribution of the dose deposited by the proton beam, that is recorded in the “Dose.out” file.

From the introduction, we know that a proton beam deposits dose as it travels through the phantom with a lowest dose delivered at the start of the beam path, and deposits most of the dose at the Braggs peak. Here, we show an example of the dose deposited and measured from the simulation.

The absorbed dose in gray was calculated and recorded within the GEANT4 simulation. Fig. 5 presents a 1.5 mm 2-D slice of a 3-D matrix of the dose deposited after passing 10 million protons of energy 150 MeV through a water phantom. The 3D volume matrix of the phantom was separated into 200 equal 2-D sheets of 1.5 mm thickness, and the slice presented in Fig. 5 was taken from the middle (15 cm mark) of the 30 cm water phantom block.

Based on Fig. 5, it can be observed that the dose distribution matches the Bragg peak expected of a proton beam, and the beam profile follows a gaussian distribution, where most of the protons are delivered from the centre of the beam. The Bragg peak occurs at 156 mm into the water phantom, and deposits a maximum dose concentration of 17.4 mGy in a 1.5 mm x 1.5 mm x 1.5 mm voxel and a total absorbed dose of 67.5276 Gy in the whole 3D phantom. Though the total absorbed dose is high, it is close to the total cumulative dose a patient often receives for a typical epithelial cancer treatment. In practice, the dose would be fractioned into smaller doses and delivered over a period of

time[1]. However, to simplify the calculation, we used 10 million proton counts in the simulation to reflect the total neutrons that will be produced over the whole course of treatment.

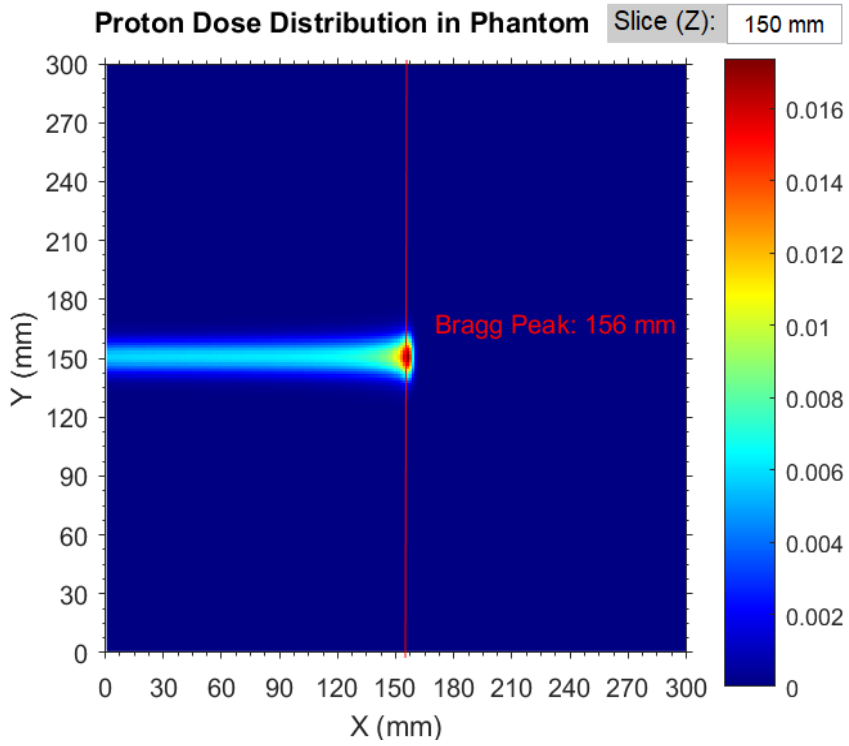


**Fig. 5.** Dose distribution from a 150 MeV proton beam containing 10 million protons passing through a water phantom taken at slice Z = 150 ± 0.75 mm. Brag peak is observed at 156 mm. Colour represents dose (gray) deposited in each 1.5 mm x 1.5 mm x 1.5 mm voxel. The total absorbed dose in the phantom is 67.5276 Gy.

In addition to the observations above, a fall off dose can be observed in Fig. 5 at the distal end of the Bragg peak. We can also see that the width of the beam profile is relatively thin along the beam path and widens when the beam is close to the region of the Bragg peak.

The widened dose profile at the region of the Bragg peak can be attributed to the higher elastic scattering interaction cross section of the low energy protons in that region,

[1] It is important to note that in real situations, the DNA repair mechanism in a cell is an important factor to consider when determining the risk of secondary cancer.

essentially due to an increase in multiple Coulomb scattering cross-section. Having a higher interaction cross section would mean that the protons undergoes more elastic nuclear scattering events, hence changing the direction of the protons and depositing dose in a wider area [7]. This contrasts with the start of the proton beam path, where the protons have a higher energy, and have a lower elastic scattering cross section. Moreover, most of the interaction at the start of the proton beam path involves electron scattering, which does not change the direction of the protons, or non-elastic nuclear scattering where the proton is absorbed into the nucleus [7].

## 3.2 Spatial Distribution of Neutrons

After looking at the dose distribution, we looked at the spatial distribution of the secondary neutrons. As mentioned in chapter 2, the 3D spatial coordinates of the secondary neutrons were recorded at the moment of production, and the track transporting the neutron was terminated right after a neutron is produced. This is done to reduce computing power and memory space of the data recorded.

Results presented in this section were obtained from passing a 150 MeV proton beam through a water phantom. From section 3.1, we know that the Bragg peak of the 150 MeV proton beam is located at the 156 mm mark into the water phantom.

From Fig. 6, we can observe that the number of secondary neutrons produced is high at the start of the proton beam path and the number tapers down as the proton beam loses energy and travels deeper into the phantom. There are very little secondary neutrons produced at the Bragg peak region of the proton beam.

This is logical as the production of secondary neutrons is a nuclear interaction that requires a threshold energy to bypass the potential from the positively charged atomic nucleus. At the start of the proton beam path, the protons generally have sufficient energy to overcome the potential barrier of the positively charged nucleus. However, as the proton travels deeper into the phantom and loses kinetic energy, the protons would have insufficient energy to break through the potential barrier of the nucleus.

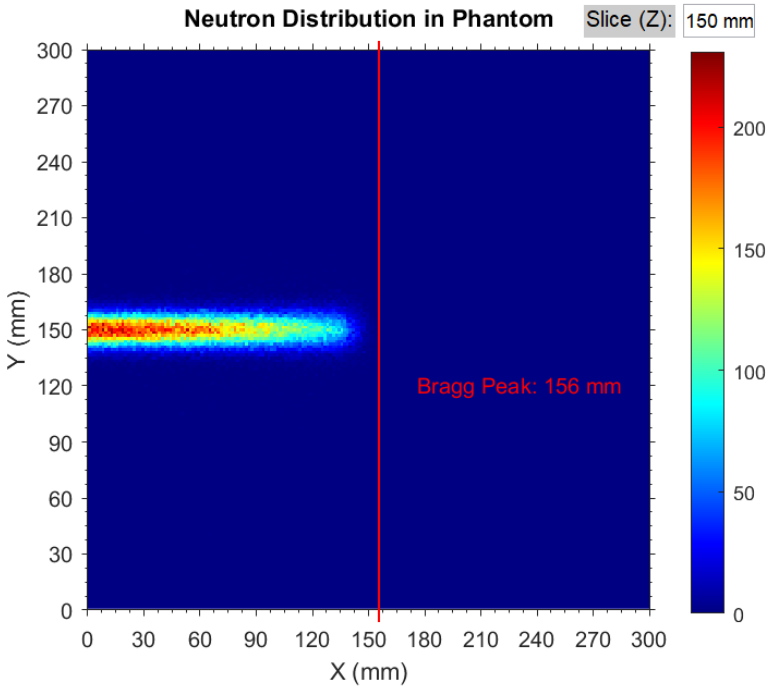


**Fig. 6.** Image of the spatial distribution of the neutrons produced in a water phantom, with proton beam containing 10 million protons with energy 150 MeV taken at slice Z = 150 ± 0.75 mm. The colour represents the total counts of neutrons in a 1.5 mm x 1.5 mm x 1.5 mm voxel.

When we compare the Bragg peak region in Fig. 5 and Fig. 6, we can see that although a high amount of is dose deposited in the Bragg peak region, only a few neutrons are produced at that region. This supports the claim that the dominant interaction of the protons at the Bragg peak region is elastic nuclear scattering instead of non-elastic nuclear scattering of the protons.

## 3.3 Spatial Distribution of the Neutron Energies

Next, we proceeded to look at the distribution of the energy of the neutrons as proton beam travels through the water phantom. This will allow us to analyse the energies of the neutrons produced in different spatial regions of the phantom as the proton beam travels through it. Results presented in Fig. 7 were obtained by finding the average energies of the neutrons that were produced in each voxel, while the sum of the energies of all the neutrons produced in each voxel are presented in Fig. 8.

The values for Fig. 7 were calculated by dividing the total energy of the neutrons from each voxel by the total neutron counts in each voxel,

$$E_i = \sum_n \frac{E_{n,i}}{N_i} \tag{4}$$

where $E_i$ is the average energy in the $i$-th voxel, $N_i$ is the neutron count in the $i$-th voxel and the sum of $E_{n,i}$ is the total energy of the neutron produced in the $i$-th voxel.

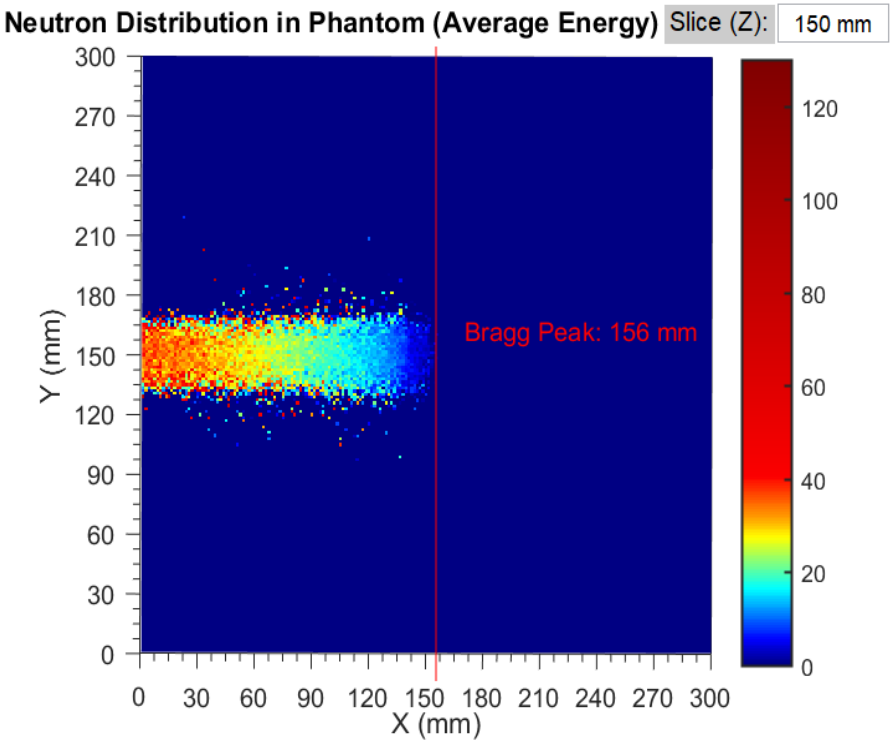


**Fig. 7.** Average energies of the neutrons in each 1.5 mm x 1.5 mm x 1.5 mm voxel taken at slice Z = 150 ± 0.75 mm for proton beam containing 10 million protons of energy 150 MeV through a water phantom. The colour represents the average energy of the neutrons in each voxel.

From Fig. 7, we can observe that there is no y-axis dependence on the average energy of the neutrons. i.e. The neutrons have a similar average energy across the y-axis.

We can also see that the average energy of the neutrons produced at the start of the proton beam path is higher than that of those closer to the Bragg peak. The average energy of the neutrons at the start of the proton beam is about 40 MeV and decreases slowly as the proton beam travels deeper, up till the depth close to the Bragg peak,

where the average energy of the neutrons is close to 0 MeV. This is because the protons have a higher energy at the start of the proton beam path as compared to the end, hence it is likely that more secondary neutrons of a high energy are produced at the start of the beam than at the end of the beam path.

However, it is important to note that the average energy here only gives us a sense of the relative energies of the neutron along the beam path, and not the actual representation of the distribution of the neutron energies. This is because the distribution is skewed, and the average of the distribution is not a good representation for a skewed distribution. More information can be found in section 3.4.

Fig. 8 was then plotted for the reader to have an overall picture of the total distribution of the neutron energy within the water phantom.

In Fig. 8, we see a trend where the total energy of the neutron is high at the start and lower in the region closer to the Bragg peak. This is due to the high neutron count and higher average energy of the neutrons at the start, compared to the end of the beam path.

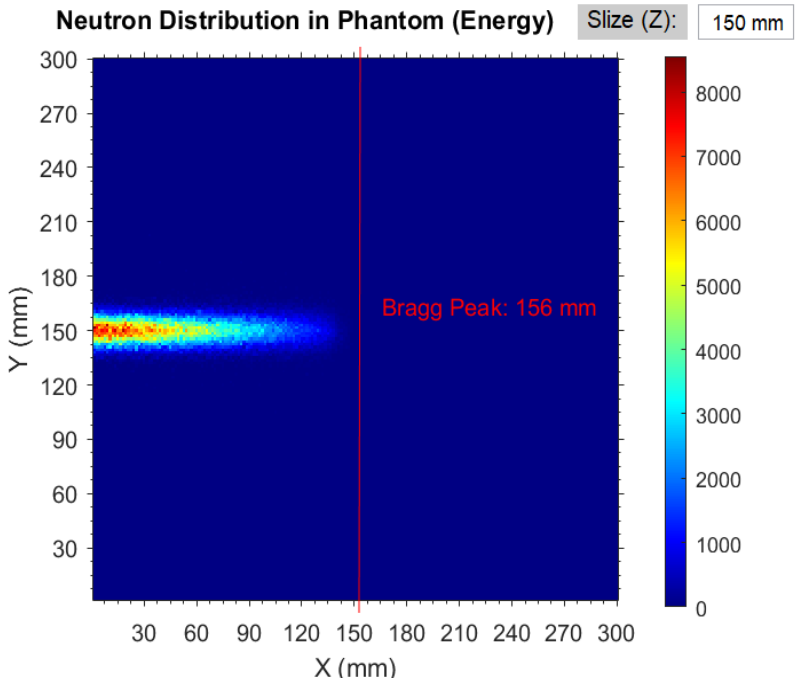


**Fig. 8.** Spatial distribution of the energies of the neutrons produced in a water phantom, with proton beam containing 10 million protons with energy 150 MeV taken at slice Z = 150 ± 0.75 mm. The colour represents the sum of energy of the neutrons in a 1.5 mm x 1.5 mm x 1.5 mm voxel.

From the plots in this section, we can see that there is a higher concentration of neutrons produced at the start of the proton beam path. This is concerning because the healthy cells located in the region will be affected by these neutrons.

In the next section, we will look at the distribution of the neutrons in terms of energy. This will allow us to understand more about the type of neutrons that are produced.

## 3.4 Energy Distribution of Neutrons

In the previous section, we have seen the average energy of the neutrons and the location it is produced. Previously, the average energy of the neutrons can give us a sense of the where high energy neutrons are distributed. However, because we are dealing with a skewed distribution, knowing only the average energy of the neutron will not give us the full picture of the type of neutron we are dealing with. This section fulfils that by showing the number of neutrons produced at each energy range. The data is presented in Fig. 9.

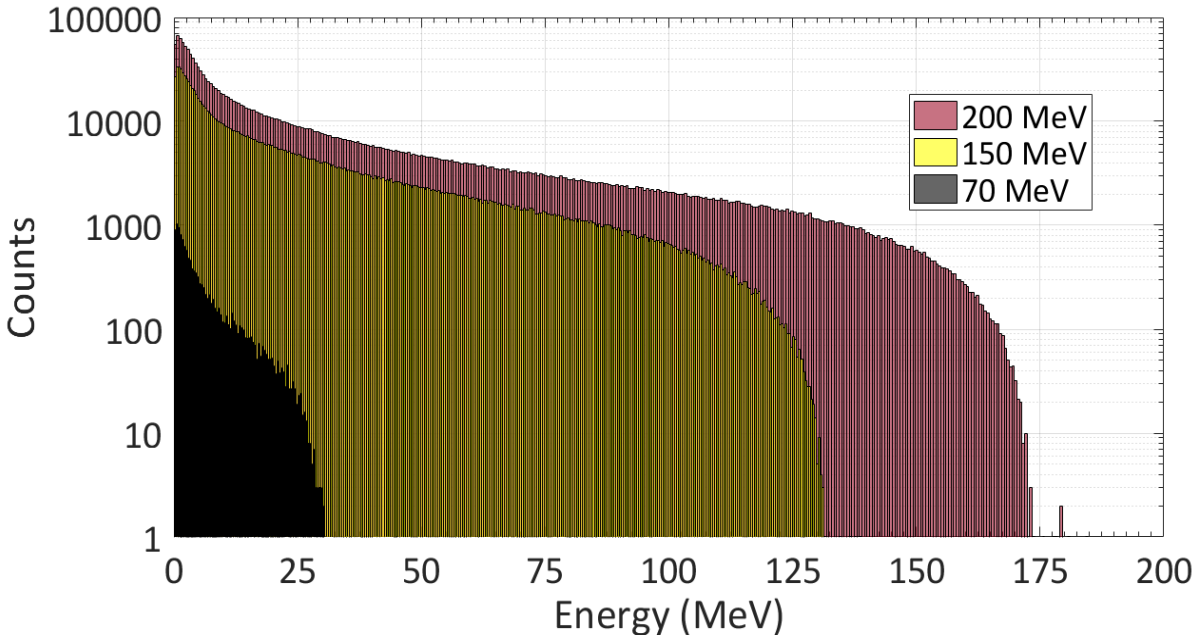


**Fig. 9.** Log-scaled histogram of the energy of neutrons produced from an incident proton beam containing 10 million protons each of energy 70 MeV, 150 MeV and 200 MeV in a water phantom with a bin width of 1 MeV.

Fig. 9 shows that when protons of energies 70 MeV, 150 MeV and 200 MeV interact with water, most of the secondary neutrons produced are neutrons of energies less than 10 MeV. From Fig. 9, the mode of the energy distribution of the neutrons are (0.6 ± 0.05) MeV, (0.8 ± 0.05) MeV and (0.6 ± 0.05) MeV respectively. For the analysis, the mode of the energy distribution was recorded, because the energy of the neutrons is too skewed to the lower energy spectrum, and therefore the mean of the distribution will not provide any useful information.

Referring back to Fig. 3, we can see that neutrons with energies from 0.1 MeV to 10 MeV have a high RBE and LET value [13]. This means that majority of the secondary neutrons produced in our simulation are lethal neutrons, and thus the effect of secondary neutron dose on biological materials should not be neglected. This serves as an additional motivation to understand more about the production of secondary neutrons in proton therapy.

Next, we explore the angular distribution of the neutrons. This will allow us to have a better understanding of where the neutrons are heading towards, and direct the proton beam such that we can avoid bathing sensitive tissues with dangerous neutrons during a treatment.

## 3.5 Angular Distribution of Neutrons

The angular distribution of the neutrons was calculated based on the momentum vector of the neutrons recorded in the GEANT4 simulation. In this section, we will be looking at the distribution of the two angles described in Section 2.4. Fig. 10 shows the distribution of $\theta$ calculated using Eq. (1) while Fig. 11 shows the distribution of $\phi$ calculated using Eq. (2). The angle $\theta$ is calculated from the propagation vector of the proton beam. i.e. an angle of $0^{\circ}$would mean that the secondary neutron is moving in the same direction as the proton beam. A visual representation the angles can be found in the appendix.

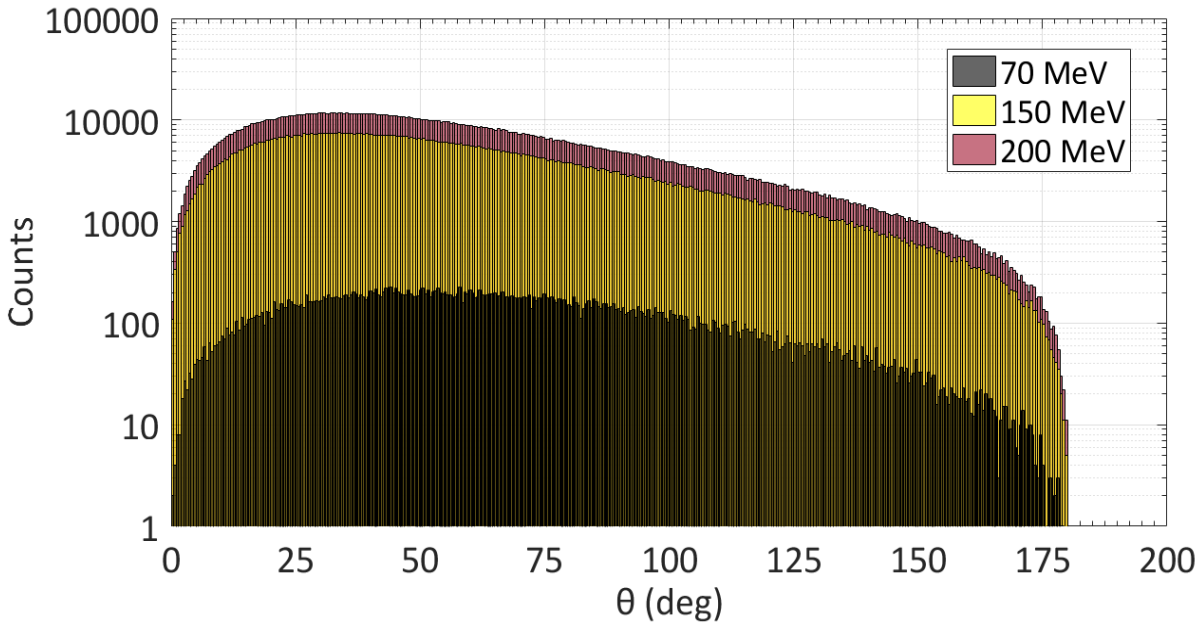


**Fig. 10.** Log-scaled histogram of the angular distribution of neutrons in the θ direction, produced from an incident proton beam containing 10 million protons each of energy 70 MeV (grey), 150 MeV (yellow) and 200 MeV (pink) in a water phantom with a bin width of 1 deg.

In Fig. 10, majority of the neutrons produced are forward facing (< 90˚), with the mode angle θ of (44.0 ± 0.05)˚for a 70 MeV proton beam, (34.8 ± 0.05)˚for a 150 MeV proton beam and (32.6 ± 0.05)˚for a 200 MeV proton beam. We see that the neutrons have a preferential angle, and a lower energy proton beam will produce neutrons that are more isotropic (histogram resembles a uniform distribution).

The preferential angle in which the neutrons are emitted, is determined by the physics model used. Currently, the binary cascade model used in the simulation agrees with experimental studies on heavy elements (Al, Fe, Pb), however no experimental studies have been done to investigate the angular distribution of the neutrons in soft tissues during proton therapy treatment. Measurements of the angular spread should be considered for the results to be conclusive.

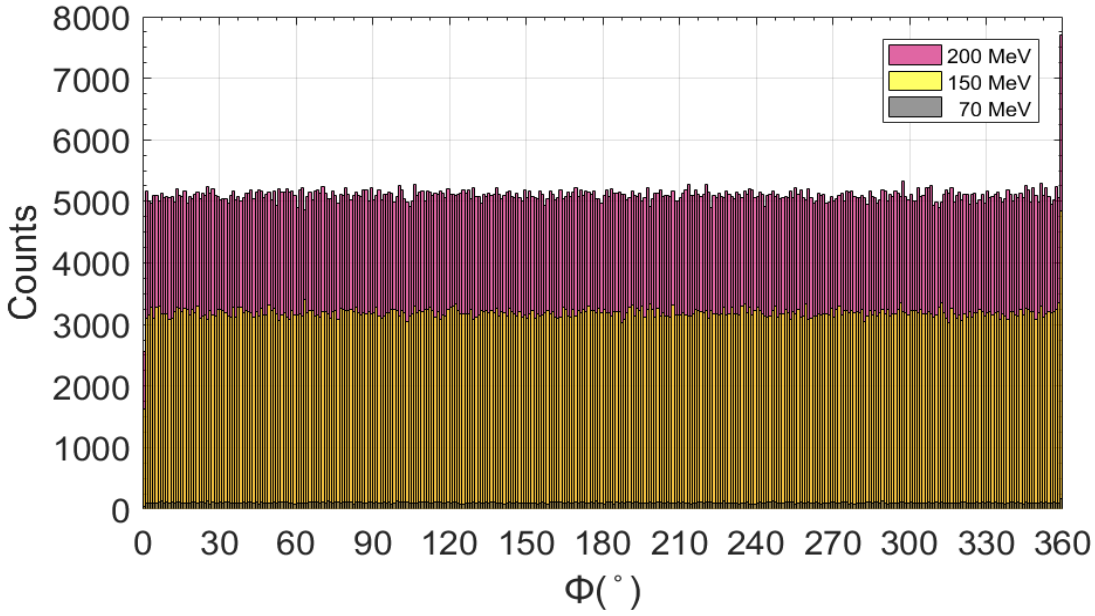


**Fig. 11.** Histogram of the angular distribution of neutrons in ϕ direction, produced from an incident proton beam containing 10 million protons each of energy 70 MeV (grey), 150 MeV (yellow) and 200 MeV (pink) in a water phantom with a bin width of 1 deg.

From Fig. 11, we can see that the neutrons are distributed in an isotropic manner in the ϕ direction for all three proton beam energies. Combining the results from Fig. 10 and Fig. 11, we can imagine the neutrons propagating in the forward direction at an angle in the shape of a ring.

After looking at the results from passing the proton beam through water and understanding how the results from each part is analysed, the next section will present a summary of the results obtained by passing the proton beam through the varying tissue medium.

## 3.6 Varying Tissue Medium

In this section, we will present a summary of the results shown in Section 3.2-3.5, in a table form, but changing the water phantom to various tissue phantoms. The total neutron counts, mode of the angle θ and the mode of the energy for the 70 MeV, 150 MeV and 200 MeV proton beam through 24 different tissue phantoms will be shown here. Table 2 contains information on the total neutron counts, while Table 3 presents the mode of the angle and the energy.

**Table 2.** The total neutron counts produced from 10 million protons of energy 70 MeV, 150 MeV and 200 MeV in the 24 different tissue phantoms used in the study.

| Tissue Name | Total Counts | | |
|---|---|---|---|
| | 70 MeV | 150 MeV | 200 MeV |
| G4 A150 Tissue | 239156 | 1158298 | 1990031 |
| G4 Adipose Tissue | 237407 | 1135662 | 1955935 |
| G4 Air | 242538 | 283779 | 294273 |
| G4 B100 Bone | 254812 | 1303740 | 2266731 |
| G4 Blood ICRP | 246252 | 1212345 | 2100267 |
| G4 Bone Compact ICRU | 253271 | 1293019 | 2256824 |
| G4 Bone Cortical | 262504 | 1387520 | 2440265 |
| G4 Brain | 245102 | 1197371 | 2070665 |
| G4 C552 Tissue | 282037 | 1569234 | 2713302 |
| G4 Eye Lens ICRP | 246540 | 1217910 | 2103334 |
| G4 Lung ICRP | 245298 | 1208021 | 2093665 |
| G4 MS20 Tissue | 246638 | 1221250 | 2107505 |
| G4 Muscle Skeletal ICRP | 245660 | 1210345 | 2094931 |
| G4 Muscle Striated ICRU | 246011 | 1211127 | 2095187 |
| G4 Muscle Without Sucrose | 246502 | 1211692 | 2092077 |
| G4 Muscle With Sucrose | 245365 | 1216236 | 2101870 |
| G4 Skin ICRP | 245405 | 1208162 | 2088722 |
| G4 Testes ICRP | 245657 | 1207585 | 2084714 |
| G4 Tissue Methane | 241173 | 283016 | 293898 |
| G4 Tissue Propane | 241884 | 285617 | 296279 |
| G4 Tissue Soft ICRP | 243547 | 1193732 | 2059839 |
| G4 Tissue Soft ICRU | 245995 | 1212557 | 2097319 |
| G4 Urea | 271717 | 1339795 | 2265090 |
| G4 Water | 244133 | 1176985 | 2078753 |

From Table 2, we can see that on average, the neutron production rate is 0.0249 neutrons/proton for 70 MeV proton beam, 0.1123 neutrons/proton for 150 MeV proton beam and 0.1918 neutrons/proton for 200 MeV proton beam. The tissue phantom that produces the most number of secondary neutrons is the C552 Tissue phantom, while the tissue phantom that produced the least number of secondary neutrons is Adipose Tissue, excluding Air, Methane and Propane.

The results seem to suggest that there is minimal linear co-relation between the total neutron fluence and the density of the material. This is expected because neutrons are produced through non-elastic nuclear interaction, which has a higher dependency on the

atomic number of the atom rather than the density of the material. A graph of the total fluence vs density of material is presented in Fig. 12.

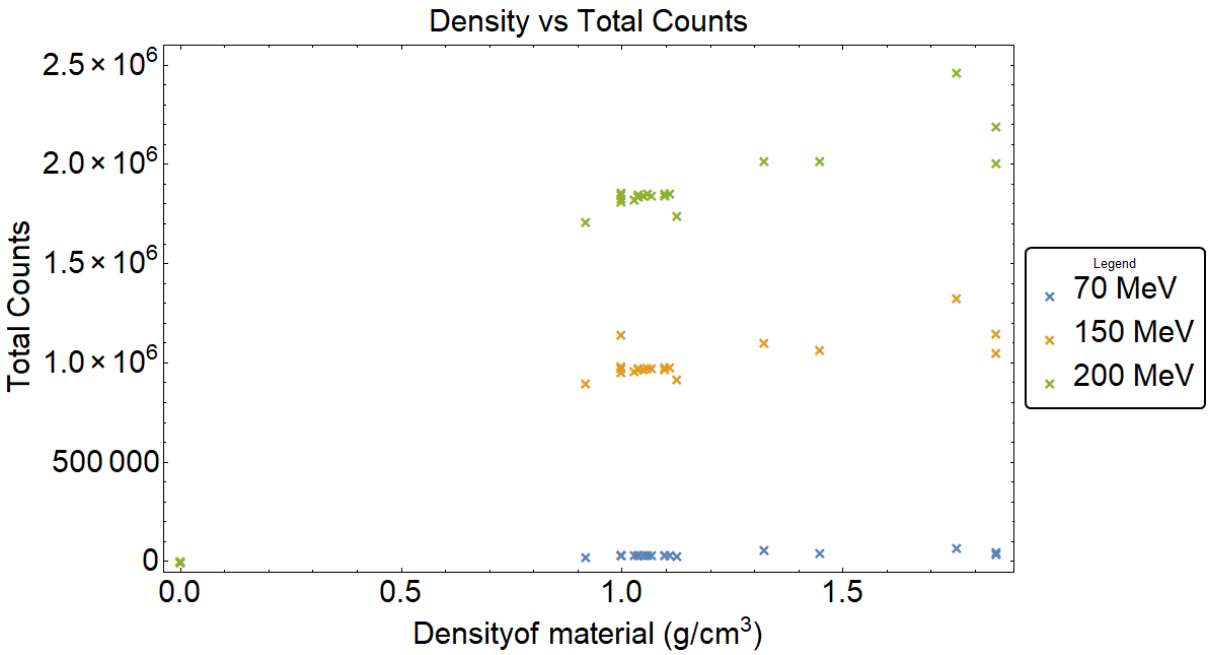


**Fig. 12.** Graph correlating the density to the total secondary neutron counts produced from proton beam energy 70 MeV (Blue), 150 MeV (Orange) and 200 MeV (Green).

A reasonable explanation for the minimal linear co-relation can be due to the different penetration depth of the protons in the different materials. Since the penetration depth of the proton beam is dependent on the slowing of a proton, and the slowing of a proton is an electronic interaction, it is reasonable to say that the density affects the penetration depth, and hence the neutron count.

A difference in secondary neutron count can also be observed when comparing the total counts between the proton beams of different energies. A higher energy proton beam produces a larger number of neutrons, and it is most probably a result of a longer beam path for a higher energy proton beam.

Table 3 shows the preferential angle and the mode energy in which the secondary neutrons are emitted. In Table 3, the variations in preferential angle is a result of the different atomic composition of the tissue cells. With this information, treatment planners can better understand the areas with a higher risk of neutron doses.

**Table 3.** The mode of the angular distribution of the neutrons (uncertainty of ± 0.05˚) and mode of the energy of the neutrons (uncertainty of ±0.05 MeV) produced from 70 MeV, 150 MeV and 200 MeV proton beam in the 24 materials used in the study. (*) represents materials where results are not statistically significant due to the low number of counts.

| | 70 MeV | | 150 MeV | | 200 MeV | |
|---|---|---|---|---|---|---|
| Tissue Name | Mode Angle (±0.05deg) | Mode Energy (±0.05MeV) | Mode Angle (±0.05deg) | Mode Energy (±0.05MeV) | Mode Angle (±0.05deg) | Mode Energy (±0.05MeV) |
| G4 A150 Tissue | 48.3 | 0.7 | 31.1 | 0.7 | 30.3 | 0.9 |
| G4 Adipose Tissue | 44.3 | 0.6 | 32.0 | 0.9 | 34.0 | 0.7 |
| G4 Air * | 26.7 | 1.1 | 55.6 | 0.6 | 32.5 | 1.7 |
| G4 B100 Bone | 35.7 | 0.5 | 33.4 | 0.8 | 33.4 | 0.7 |
| G4 Blood ICRP | 56.4 | 0.4 | 35.6 | 0.6 | 34.9 | 0.8 |
| G4 Bone Compact ICRU | 43.9 | 0.6 | 29.1 | 0.6 | 31.9 | 0.7 |
| G4 Bone Cortical | 50.0 | 0.7 | 33.0 | 0.6 | 32.8 | 0.7 |
| G4 Brain | 44.7 | 0.6 | 32.0 | 0.6 | 30.0 | 0.8 |
| G4 C552 Tissue | 45.9 | 0.7 | 30.7 | 0.7 | 35.0 | 0.7 |
| G4 Eye Lens ICRP | 57.6 | 0.7 | 26.9 | 0.9 | 33.3 | 0.8 |
| G4 Lung ICRP | 47.8 | 0.5 | 37.1 | 0.8 | 27.6 | 0.8 |
| G4 MS20 Tissue | 38.4 | 0.7 | 29.0 | 0.7 | 34.1 | 0.8 |
| G4 Muscle Skeletal ICRP | 57.2 | 0.6 | 32.0 | 0.7 | 31.0 | 0.8 |
| G4 Muscle Striated ICRU | 53.9 | 0.9 | 34.5 | 0.6 | 28.9 | 0.6 |
| G4 Muscle Without Sucrose | 38.4 | 0.4 | 32.2 | 0.7 | 34.2 | 0.8 |
| G4 Muscle With Sucrose | 46.4 | 0.8 | 33.0 | 0.8 | 30.6 | 0.7 |
| G4 Skin ICRP | 34.7 | 0.7 | 34.1 | 0.9 | 34.4 | 0.7 |
| G4 Testes ICRP | 38.6 | 0.7 | 35.9 | 0.8 | 31.6 | 0.9 |
| G4 Tissue Methane * | 104.0 | 0.8 | 38.7 | 0.3 | 28.5 | 3.1 |
| G4 Tissue Propane * | 33.9 | 0.4 | 18.0 | 0.9 | 17.6 | 2.0 |
| G4 Tissue Soft ICRP | 40.8 | 0.7 | 35.4 | 0.8 | 37.1 | 0.7 |
| G4 Tissue Soft ICRU | 57.9 | 0.6 | 31.9 | 0.8 | 29.2 | 0.7 |
| G4 Urea | 45.6 | 0.6 | 34.1 | 0.8 | 33.0 | 0.8 |
| G4 Water | 44.0 | 0.6 | 34.8 | 0.8 | 32.6 | 0.6 |

In table 3, it is also notable that most of the neutrons produced are intermediate neutrons, with energies of about 0.7 MeV to 0.9 MeV. The mean free path of such neutrons is about 6.3 cm in water. This is calculated from the total scattering interaction cross section of neutrons with Hydrogen-1 (4.79 ± 0.11 barns for 0.798 ± 0.008 MeV neutrons) [21].

Having a mean free path of 6.3 cm may seem long, however the average male human has a waist circumference of 39.7 inches [22], and most of the secondary neutrons produced are forward facing. This means if the proton beam was treating a deep-seated tumour within the body, the neutrons generated would have interacted with most of the body and deposited out-of-field doses into the body.

From the above sections, we have shown and emphasized on the importance of considering neutron doses when creating a treatment plan for a patient. In the next section, we will quantify the relative risk of biological damage among different tissues, using the lethality factor defined in Section 2.5. We will then be comparing the lethality factors across different tissue mediums to identify the tissues that produces the most lethal neutrons.

## 3.7 Lethality

Two methods were used to compare the lethality of the neutrons produced in the different tissue phantoms. In the first method, we plot the spatial distribution of the lethality factors based on the calculations stated in Section 2.5. We then record the lethality factor of the voxel with the highest lethality factor and compare the value recorded when using different tissue phantoms. Results from this method is presented in Fig. 13. For the second method, the sum of the lethality factor of all the voxels in the phantom was recorded and used as a comparison for different tissue phantoms. This is presented in Fig. 14.

The first plot in Fig. 13 shows the concentration of the lethality of the neutrons across the different tissues. This removes the bias caused by the different penetration depth of the proton beam through different tissue mediums. The next graph in Fig. 14 gives an overview of the overall lethality of the neutrons produced in different tissues.

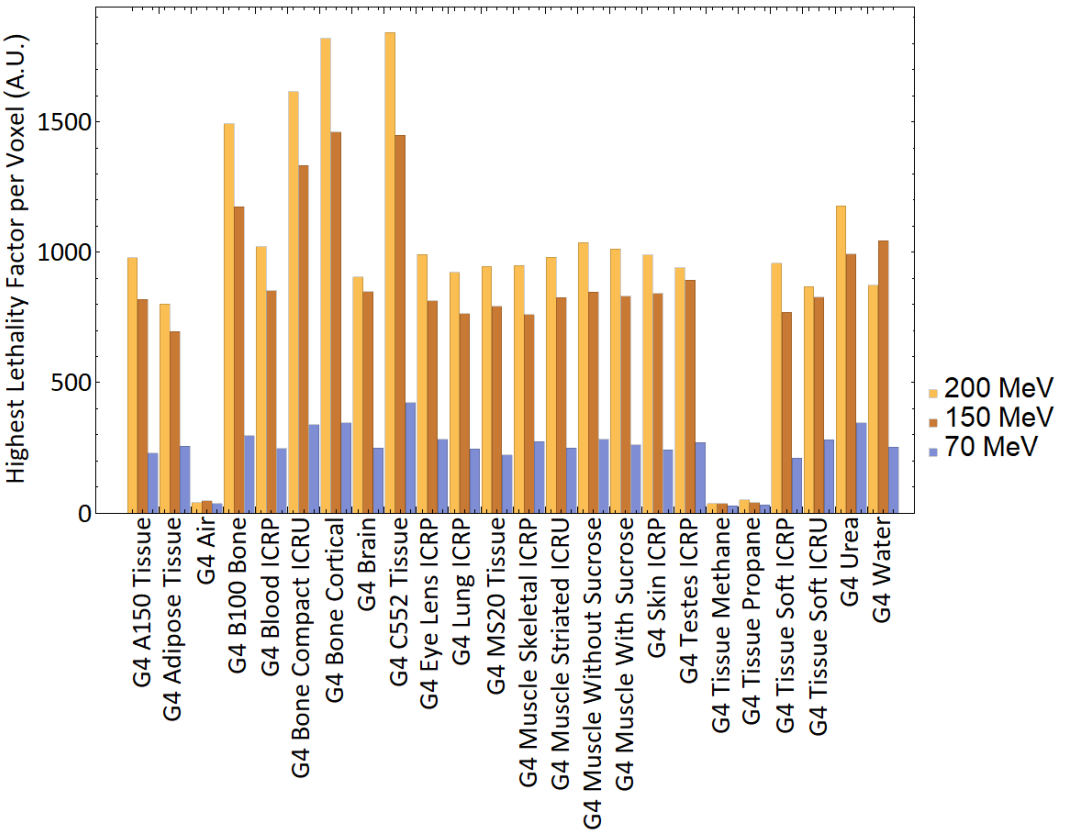


**Fig. 13.** Bar chart showing the highest lethality factor of neutrons produced from 70 MeV (blue), 150 MeV (brown) and 200 MeV (orange) proton beam. The 24 materials used in this study are shown in the chart.

Fig. 13 shows a non-trivial relation of the possible localized lethality of the neutrons between the different tissue models, and it serves as a motivation to investigate the maximum risk of damage from transport of the neutrons.

The lethality factor shown in Fig. 13 is a measure of the localized risk at the point of production. In Fig. 13, you can also observe that tissues such as B100 bone equivalent tissue, bone compact, bone cortical and C552 air equivalent tissues. A common factor between the bone tissues are the high calcium content in the tissues [4]. This might be a result of the high Ca(p,n)Sc cross-section of Calcium-44 [23]. Although C552 tissue is an air equivalent plastic that has no calcium content, it is suspected that the high neutron count can be attributed to the high Fluorine composition [4].

This suggest that one should avoid directing the proton beam through tissues with high Calcium and Fluorine content, such as bone tissues.

Next, the total lethality factor is presented to give the reader a sense of the total relative risk of DNA damage from the production of secondary neutrons in different tissue medium.

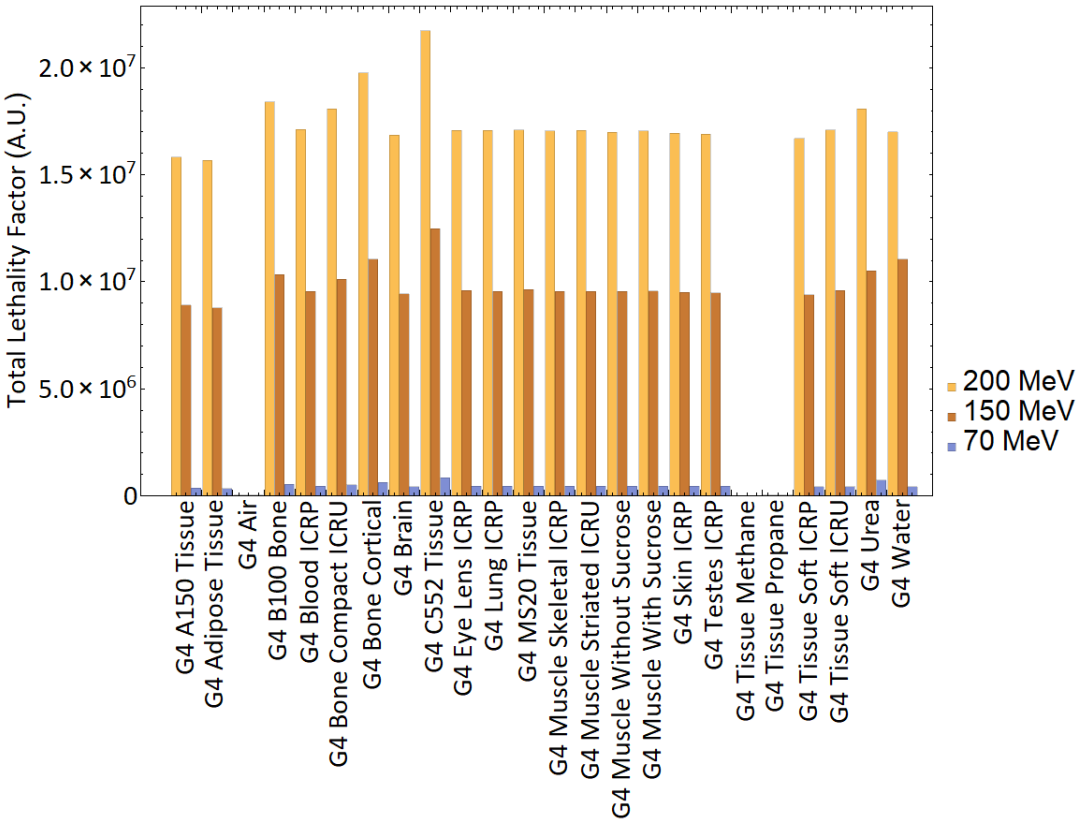


**Fig. 14.** Bar chart showing the highest lethality factor of neutrons produced from 70 MeV (blue), 150 MeV (brown) and 200 MeV (orange) proton beam. The 24 materials used in this study are shown in the chart.

In Fig. 14, we can see a trend where the Bone tissues and C552 tissue has a high lethality factor as compared to the other tissues that have similar lethality factors. The slight difference in trend seen in Fig. 13 and Fig. 14 might be because Fig. 14 shows the total lethality, and does not correct for the difference in penetration depth.

From the information in chapter 3, we can better understand the properties of the secondary neutrons produced in proton therapy. In the next few chapters, we compare different physics models that can be used in the simulation. We will also introduce a short chapter on the transport of the neutrons within the phantom. This will allow us to have a clearer picture of what happens to the neutrons after production, and possible continuation of the project.

# 4 Comparison between Physics Models

Considering that we have identified the tissues that generates the highest number of lethal neutrons, we now investigate the validity of the physics model used in the simulation. This will be done through a comparison between two possible physics models in GEANT4, the Bertini model (BERT) [20] and the Binary Cascade model (BIC) [20]. In addition, the comparison also includes the difference between a model with the addition of the neutron high precision (HP) model [20] and without it. This serves as a test to see how the addition of the HP model will affect the results recorded.

In this chapter we have only included results obtained from passing a 150 MeV proton beam through a water phantom. The total neutron count, mode and mean of the angle and energy of the secondary neutrons, generated from running different physics models, are presented in Table 4.

**Table 4.** Table comparing the total count, mean and mode of the angle and energy of the secondary neutrons produced from simulation running on different physics models (BERT, BERT + HP, BIC, BIC + HP).

| Physics Model | Total Neutron Count | Mean Angle (˚) | Mode Angle (˚) | Mean Energy (MeV) | Mode Energy (MeV) |
|---|---|---|---|---|---|
| BERT | 977726 | 69.7 | 41.1 | 16.17 | 0.80 |
| BERT + HP | 977725 | 69.7 | 41.1 | 16.17 | 0.80 |
| BIC | 1199177 | 57.5 | 34.4 | 23.09 | 0.70 |
| BIC + HP | 1199175 | 57.5 | 34.4 | 23.09 | 0.70 |

From Table 4, we can see that there is only a slight difference between using the physics model with and without the addition of the HP model. When comparing the physics model with and without the HP model, the total neutron counts only varied by a percentage difference of 0.00008%, while the angular and energy distribution of the neutrons were not affected. It is expected to observe no difference with the addition of

the HP model because the HP model is meant for the transport of the neutrons. Since the neutrons were not transported in experiment, no difference should be observed. The slight variation in neutron count between the model with and without the addition of the HP model can be attributed to the randomness of a Monte-Carlo simulation.

However, when comparing between the BERT model and the BIC model, a percentage difference of 10.2% for the total neutron count, 9.59% and 8.74% for the mean and mode angle respectively, 17.6% and 6.67% for the mean and mode energy respectively can be observed.

The angular distribution of the neutrons and the energy distribution of the neutrons is presented in Fig. 15 and Fig. 16 respectively, to have a clearer illustration of the difference between the two physics models.

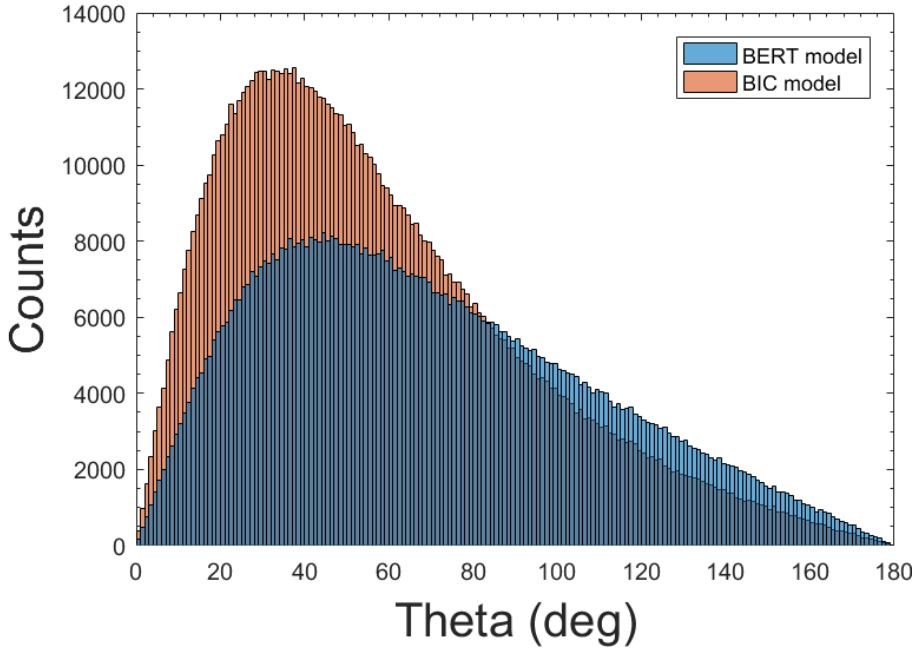


**Fig. 15.** Histogram of the angular distribution of neutrons in the θ direction, produced from an incident proton beam containing 10 million protons each of energy 150 MeV in a water phantom with a bin width of 1 deg. The two histograms represent the two physics model, BERT (blue) and BIC (orange) used for comparison.

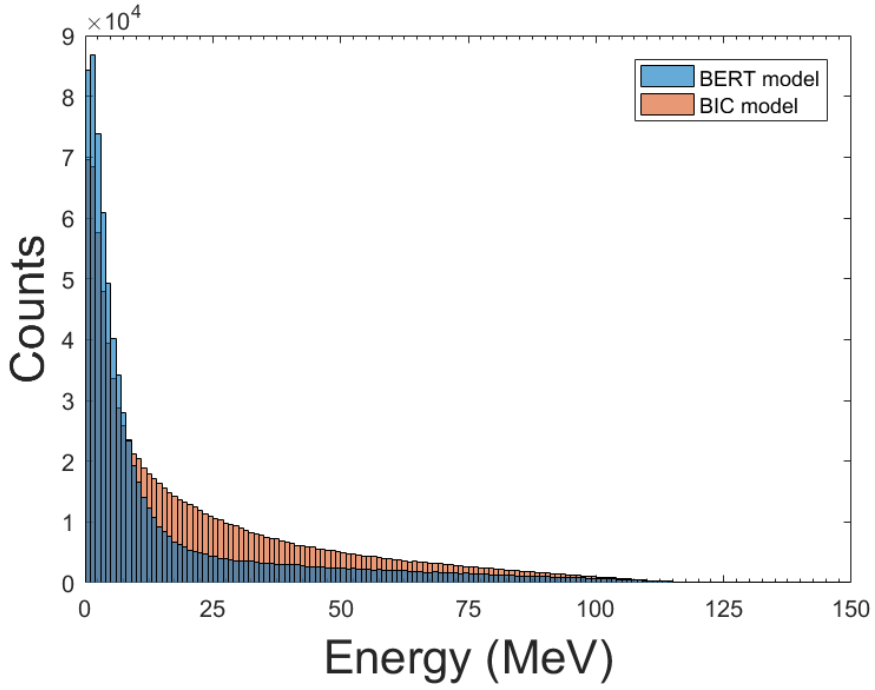


**Fig. 16.** Histogram of the energy distribution of neutrons produced from an incident proton beam containing 10 million protons each of energy 150 MeV in a water phantom with a bin width of 1 MeV. The two histograms represent the different physics model, BERT (blue) and BIC (orange) used for comparison.

In Fig. 15, you can see that the BERT model generates neutrons in a more isotropic manner as compared to the BIC model. This is evident from the broader width of the histogram. In Fig. 16, you can see that the energy distribution of the neutrons from the BERT model is more skewed towards the lower energy range as compared to that from the BIC model. These differences can be attributed to the different algorithms used in each physics model.

The BERT model simulates inelastic scattering through an intra-nuclear cascade developed by Bertini [20]. This intra-nuclear cascade solves the Boltzmann equation on the average to obtain details of the physical collision process. The target nucleus used in this model is a smooth nuclear medium where particle-hole states are added after each interaction. The states of each interaction are determined according to the cross-section data in GEANT4. At the end of the cascade, the excited nucleus, which consists of the sum of states from the interactions, decays through pre-equilibrium, evaporation methods, fission or nucleus explosion into the final products [24].

The BIC model also simulates inelastic scattering through an intra-nuclear cascade model like the BERT model [20]. However, in this model, the target nucleus in the BIC model is made up of a 3-D collection of nucleons, instead of a smooth nuclear medium. The interaction between the nucleus and the incident particle is modelled through a series of two-particle collisions of the nucleons in the 3-D model. The rate of interaction is determined by the interaction cross section of the particles in the GEANT4 database. Secondary particles are created during the decay of the excited nucleus, handled by the G4Precompound Model [25].

A more isotropic angular distribution is observed in the BERT model probably because the BERT model uses evaporative and pre-equilibrium models to simulate the de-excitation of the nucleus, and both models emit particles in an isotropic manner [20]. This is compared to the BIC model, that solves for the Boltzmann-Uehling-Uhlenbeck equation to obtain the energy, momentum and angles of the particles in the scattering process.

A possible explanation of why the BERT model generates lower energy neutrons as compared to the BIC model, is the cut off energy for the intra-nuclear cascade to stop is lower for the BERT model (2MeV) as compared to the BIC model (15 MeV).

Both models are good for the energy range used in proton therapy. However, the BIC model was chosen for this study because the 3-D collection of the nucleons used in the BIC model is a better representation of a real atom. In addition, the BERT model has only been experimentally tested with bullet kinetic energies between 100 MeV to 5 GeV [20]. This contrasts with the BIC model, that has been tested for kinetic energies from 10 MeV to 1200 MeV [20], and matches the energy range used in proton therapy.

After comparing the physics models, in the next chapter, we will look at the transport of the neutrons as a short introduction on what happens to the neutrons after being produced.

# 5 Neutron Transport

In the previous chapters, we have explored the production of neutrons in proton therapy. However, to reduce computational power and data space, we have neglected the transport of the neutrons within the phantom. In this chapter, we will present a short introduction on the transport of the neutrons within the phantom. This will provide the reader with a more complete picture of the neutrons produced, and a possible consideration for the continuation of the project.

For this chapter, we reduced the number of protons per run from 10 million protons, used in the previous sections, to 100 thousand protons. This reduced the size of the data, from 20 Gigabytes/run to about 200 Megabytes/run, and made the analysis more manageable. This chapter only presents the 150 MeV proton beam incident onto a water phantom, because it serves a short introduction for future works.

The transport of the secondary neutron were simulated using the neutron high precision model in GEANT4 (HP model) [20], that considers neutron in-elastic scattering of the neutrons within the water phantom. This is presented in Fig. 17. A scenario where there is no interaction between the neutrons and the phantom was also simulated, by linearly transporting the neutrons based on its momentum. This is presented in Fig. 18.

Based on the transport of the neutrons using the HP model (Fig. 17), we can see that the secondary neutron tracks have interacted with the phantom and have possibly deposited out-of-field doses. This evident from the short and fragmented lines observed, and contrasts with the figure simulating no interaction (Fig. 18), where the neutron tracks are long and continuous.

This provides further evidence that the neutrons produced from proton therapy do not just pass through the water phantom without depositing dose, and treatment planners should consider secondary neutron doses.

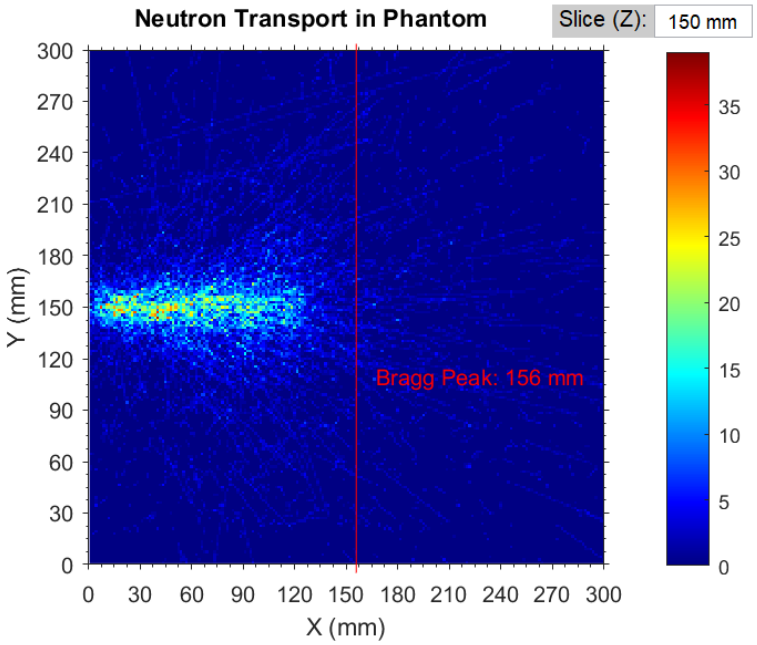


**Fig. 17.** Image depicting the track of the secondary neutrons as it travels through the water phantom simulated using the neutron high precision model in GEANT4. A proton beam containing 100 thousand protons of energy 150 MeV was used to generate the secondary neutrons. The colour bar indicates the number of times the secondary neutron passes through the voxel of size 1.5 mm x 1.5 mm x 1.5 mm.

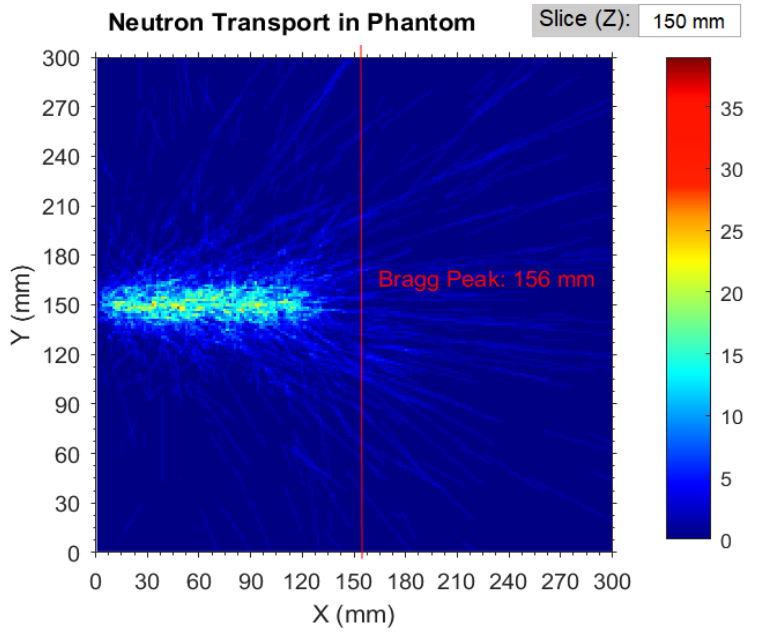


**Fig. 18.** Image depicting the track of the secondary neutrons as it travels through the water phantom simulated using MATLAB to transport the neutron in a straight line based on its momentum. A proton beam containing 100 thousand protons of energy 150 MeV was used to generate the secondary neutrons. The colour bar indicates the number of times the secondary neutron passes through the voxel of size 1.5 mm x 1.5 mm x 1.5 mm.

# 6 Conclusion

In our study, we investigated the spatial, angular and energy distribution of the secondary neutrons produced in proton therapy. The neutrons produced in proton therapy are mostly created at the start of the beam path and are propagated at a preferential direction depending on the atomic composition. Results show that most of the neutrons produced in the 24 tissue phantoms are intermediate neutrons (< 1 MeV). This is a cause for concern because the neutrons in this energy range have a high RBE value and a small mean free path relative to the size of an average human, that can result in high localized biological damage. The relative lethality factors described in this paper informs treatment planners to avoid directing the proton beam towards tissues such as bone tissues, to reduce the risk of DNA damage due to secondary neutrons. In addition, the comparison of the results between different physics models available within GEANT4 showed how the physics models affect the results. Through exploring the transport of the neutrons, we reasoned that neutron doses in proton therapy should not be neglected, and future works can be conducted on this topic.

# 7 Future Works

This is a promising field of study and it has a tremendous impact on how proton therapy treatment planners view the secondary neutrons. There are several follow-up studies that can be conducted to improve our understanding of the secondary neutrons produced in proton therapy.

First, actual measurements of the angular distributions of neutrons can be done to verify that neutrons are produced at a preferential angle. Next, optimisation of the data recording process of the neutron transport can be done, such that we can obtain a more accurate understanding of the risks involved with these secondary neutrons. The successful transport of the neutrons will show the spatial distribution of the secondary neutron dose throughout the body, and allow us to determine if the neutron count produced from proton therapy is sufficiently high for Boron-11 to act as an effective radiosensitiser and increase the dose deposited in the tumour region. Finally, changing the block phantom into an actual human phantom compromising of data input from a CT scan can have actual clinical impact.

# References


[1] S. Agostinelli *et al.*, "Geant4—a simulation toolkit," *Nucl. Instruments Methods Phys. Res. Sect. A Accel. Spectrometers, Detect. Assoc. Equip.*, vol. 506, no. 3, pp. 250–303, Jul. 2003.

[2] J. Allison *et al.*, "Geant4 developments and applications," *IEEE Trans. Nucl. Sci.*, vol. 53, no. 1, pp. 270–278, Feb. 2006.

[3] J. Allison *et al.*, "Recent developments in GEANT4," *Nucl. Instruments Methods Phys. Res. Sect. A Accel. Spectrometers, Detect. Assoc. Equip.*, vol. 835, pp. 186–225, 2016.

[4] D. Wright, "Geant4 Materials," 2016. [Online]. Available: http://geant4.web.cern.ch/geant4/workAreaUser-%0ADocKA/Backup/Docbook_UsersGuides_beta/ForApplicationDeveloper/html/apas08.html,%0Alast accessed 2018/03/07. [Accessed: 21-Mar-2018].

[5] "Introduction to Proton Beam Radiation Therapy," 2015. [Online]. Available: http://www.chang-gung.com/en/news-1.aspx?rows=8&page=1 &type=&id=352&mid=120&bid=3. [Accessed: 21-Mar-2018].

[6] "New NCCS Building and the Goh Cheng Liang Proton Therapy Centre," *National Cancer Centre Singapore*. [Online]. Available: https://www.nccs.com.sg/ABOUTUS/OURFACILITIES/Pages/NewNCCSBuildingProton%0ATherapyCentre.aspx. [Accessed: 21-Mar-2018].

[7] W. D. Newhauser and R. Zhang, "The physics of proton therapy.," *Phys. Med. Biol.*, vol. 60, no. 8, p. R155, 2015.

[8] R. V. Sethi *et al.*, "Second nonocular tumors among survivors of retinoblastoma treated with contemporary photon and proton radiotherapy," *Cancer*, vol. 120, no. 1, pp. 126–133, Jan. 2014.

[9] C. S. Chung, T. I. Yock, K. Nelson, Y. Xu, N. L. Keating, and N. J. Tarbell, "Incidence of Second Malignancies Among Patients Treated With Proton Versus Photon Radiation," *Int. J. Radiat. Oncol.*, vol. 87, no. 1, pp. 46–52, Sep. 2013.

[10] B. R. Eaton *et al.*, "Clinical Outcomes Among Children With Standard-Risk Medulloblastoma Treated With Proton and Photon Radiation Therapy: A Comparison of Disease Control and Overall Survival," *Int. J. Radiat. Oncol.*, vol. 94, no. 1, pp. 133–138, Jan. 2016.

[11] S. Agosteo, C. Birattari, M. Caravaggio, M. Silari, and G. Tosi, "Secondary neutron and photon dose in proton therapy," *Radiother. Oncol.*, vol. 48, no. 3, pp. 293–305, 1998.

[12] U. Schneider and R. Hälg, “The Impact of Neutrons in Clinical Proton Therapy,” *Front. Oncol.*, vol. 5, no. October, p. 235, Oct. 2015.

[13] G. Baiocco *et al.*, “The origin of neutron biological effectiveness as a function of energy,” *Sci. Rep.*, vol. 6, no. 1, p. 34033, Dec. 2016.

[14] National Nuclear Data Center, “Evaluated Nuclear Data File.”

[15] H. Paganetti, “Relative biological effectiveness (RBE) values for proton beam therapy. Variations as a function of biological endpoint, dose, and linear energy transfer,” *Phys. Med. Biol.*, vol. 59, no. 22, pp. R419–R472, 2014.

[16] J. D. Boice *et al.*, “The 2007 Recommendations of the International Commission on Radiological Protection,” 2007.

[17] E. J. Hall, “Intensity-modulated radiation therapy, protons, and the risk of second cancers,” *Int. J. Radiat. Oncol. Hall EJ. Intensity-modulated Radiat. Ther. protons, risk Second cancers. Int J Radiat Oncol. 2006;65(1)1-7. doi10.1016/j.ijrobp.2006.01.027.*, vol. 65, no. 1, pp. 1–7, May 2006.

[18] D. J. Brenner and E. J. Hall, “Secondary neutrons in clinical proton radiotherapy: A charged issue,” *Radiother. Oncol.*, vol. 86, no. 2, pp. 165–170, Feb. 2008.

[19] G. A. P. Cirrone *et al.*, “Implementation of a new Monte Carlo - GEANT4 simulation tool for the development of a proton therapy beam line and verification of the related dose distributions,” *IEEE Trans. Nucl. Sci.*, vol. 52, no. 1 I, pp. 262–265, 2005.

[20] D. H. Wright, “Physics Reference Manual,” *Geant4*, vol. 3, no. December, pp. 1–558, 2011.

[21] E. Lampi, G. Freier, and J. Williams, “The Total Scattering Cross Section of Neutrons by Hydrogen and Carbon,” *Phys. Rev.*, vol. 80, no. 5, pp. 853–856, 1950.

[22] Statistics Brain, “Human body statistics.” [Online]. Available: https://www.statisticbrain.com/human-body-statistics/. [Accessed: 31-Mar-2018].

[23] C. H. M. Broeders and A. Y. Konobeyev, “Systematics of (p, n) reaction cross-section,” *Radiochim. Acta*, vol. 96, no. 7, pp. 387–397, 2008.

[24] Geant4, “Bertini cascade.” [Online]. Available: http://geant4.cern.ch/support/proc_mod_catalog/models/hadronic/BertiniCascade.html. [Accessed: 31-Mar-2018].

[25] Geant4, “Binary Cascade.” [Online]. Available: http://geant4.cern.ch/support/proc_mod_catalog/models/hadronic/BinaryCascade.html. [Accessed: 31-Mar-2018].

# 8 Appendix

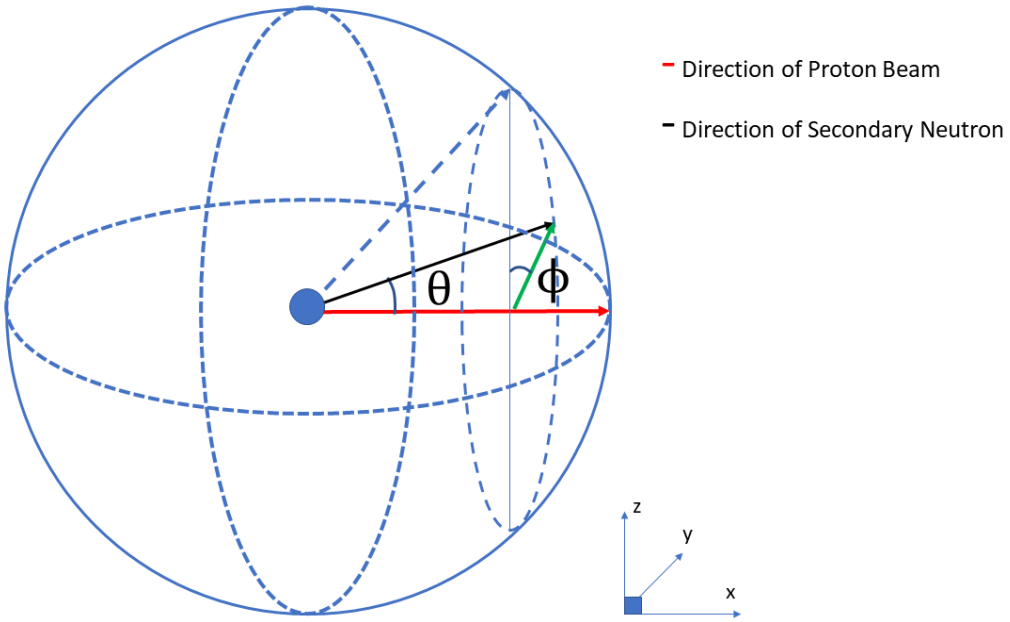


**Appendix 1.** Visualisation of the angles calculated in this thesis